Computational Materials Science 147 (2018) 154–167

Contents lists available at ScienceDirect

Computational Materials Science

journal homepage: www.elsevier.com/locate/commatsci

Mechanical properties of Au foams under nanoindentation

Carlos J. Ruestes [a,*], Daniel Schwen [b], Emmanuel N. Millán [a], Emiliano Aparicio [c], Eduardo M. Bringa [a]

[a] CONICET and Facultad de Ciencias Exactas y Naturales, Universidad Nacional de Cuyo, Mendoza 5500, Argentina
[b] Department of Fuels Modeling and Simulation, Idaho National Laboratory, Idaho Falls, ID, USA
[c] CONICET and Instituto de Bioingenieria, Universidad de Mendoza, Mendoza 5500, Argentina

ARTICLE INFO

Article history:
Received 21 November 2017
Received in revised form 1 February 2018
Accepted 5 February 2018

Keywords:
Nanofoams
Simulation
Nanoindentation
Plasticity

ABSTRACT

Nanoscale metallic foams display mechanical properties which make them attractive for a variety of technological applications. We report simulated nanoindentation tests for a model polycrystalline nanoporous gold structure with 11 nm mean filament diameter and 35 nm average grain size, comparable to foams produced by dealloying. Hardness, plasticity mechanisms, the extension of the plastic zone and the applicability of several scaling laws are discussed. Plasticity occurs at the nodes mainly and is dominated by nucleation of dislocations at the atomic steps of the ligament surfaces, in a dislocation accumulation scenario. Shockley partials, perfect dislocations, Hirth partials, Lomer-Cottrel locks and twins were identified. Grain boundary sliding appears to play a minor role in deformation at the indentation rates used. Several scaling laws are tested and their results and applicability are discussed based on the structural parameters of the foam and the deformation mechanisms identified.

1. Introduction

Nanoporous structures span over a wide variety of materials, ranging from biological materials such as feathers, bird beaks, cortical and cancellous bones [1,2], to tailored metallic nanofoams. The high surface-to-volume ratio of metallic foams place them as a first choice for catalysis applications [3–5], and have enabled cutting-edge technology such as surface-chemistry-powered actuators and sensors [6–12]. Due to their structure, potential uses extend to lightweight structural panels and energy absorption devices, among others [13].

Nanoporous gold (np-Au) is probably the most studied nanoporous metal and that is due to its easy fabrication and virtues inherited from its base material (Au), which are stability against oxidation and corrosion [14]. The properties of nanoporous Au have been explored by a variety of experimental [14–17] and modeling techniques [18–23]. Biener et al. [14] used nanoindentation tests to derive its elastic modulus and yield strength, Mathur and Erlebacher [24] relied on microtension tests for similar purposes while Bürckert et al. [25] opted for uniaxial compression testing. There is a general agreement that the mechanical properties of np-Au depend on microstructural parameters such as the ligament size, network connectivity, etc. Two recent contributions serve as examples; Viswanath et al. [26] studied the scaling behavior of hardness with ligament diameter and vacancy defect concentration in nanoporous gold using hardness measurements, scanning electron microscopy, and positron lifetime measurements. They found differences in the scaling of hardness with ligament diameter, pointing to constrained motion of dislocations as the root of this behavior. Liu and co-workers [27,28] and Mangipudi et al. [29] focused their efforts on the assessment of the role of network connectivity on mechanical properties, highlighting its importance.

Historically, the plastic collapse model by Gibson and Ashby [30] has been the first choice to estimate the elastic modulus, yield strength and ultimate tensile strength of foams, not only because it is based on the relative mass density and a few constants but also because its application to micron-scale and macroscopic porous materials was successful in matching the performance found during experimental tests. The validity of the G-A model for nanofoams is still under debate [18,25,27,31–33], the main reason being that it does not take into account many microstructural parameters of importance. For instance, evidence suggests that the ligament diameter plays a significant role in the mechanical response [31,33]. Hodge and co-workers [31] proposed a modified scaling law for the yield stress as a function of the average ligament diameter and the relative mass density. Viswanath et al. [26] proposed a scaling of the hardness with ligament diameter with an exponent of −0.3 instead of the conventional Hall–Petch exponent of −0.5 for bulk systems. Liu et al. [27,28] proposed to use the G-A model considering an effective relative density that takes into account the network connectivity.

* Corresponding author.
E-mail address: cruestes@fcen.uncu.edu.ar (C.J. Ruestes).

https://doi.org/10.1016/j.commatsci.2018.02.019
0927-0256/

Molecular dynamics (MD) studies had already provided valuable insights into the mechanical properties of np metals [18,19,34–37]. However, many MD studies are either based on highly simplified geometrical models [38] or microstructures that try to mimic those in real nanofoams but considering a single crystal with extremely thin ligaments (e.g. 2 nm to 4 nm) [18,19,21,37,36]. Single crystalline MD studies (e.g. [37]) are justified on the fact that, in general, the ligament structure has a length scale in the nanometer to micron range, whereas the base material has a grain size of tens of microns and above. Yet, electron microscopy images have revealed polycrystalline np-Au thin films where the ligament size is commensurate to the grain size and in the order of 50 nm [39,40]. The lack of computational studies in such cases is notorious and is one of the main motivations for this research.

In this paper, we present an upscaling in MD nanoindentation studies by probing a polycrystalline gold nanofoam with a mean ligament size of 11 nm. The purpose of this paper is to explore the mechanical properties, scaling laws and deformation mechanisms of nanofoams under nanoindentation conditions. Section 2 presents a detailed description of the sample, simulation setup and tools. Section 3 presents the results of the simulation and its post-processing, including load-penetration curves and hardness estimations (Section 3.1), the identification of deformation mechanisms (Section 3.2), extension of the plastic zone (Section 3.3) and a thorough comparison with available scaling laws (Section 3.4). The main conclusions are outlined in Section 4.

2. Methods

This section describes the methodology employed. A novel aspect of this work is the development of a computational domain that mimics the complex structure of nanocrystalline Au foams, its details are described in Section 2.1, while the details of the simulated nanoindentation experiment are presented in Section 2.2.

2.1. Sample generation

Nanoporous gold produced by dealloying [3] exhibits microstructures that appear as random-sized open cells [41,42], resembling those structures associated with spinodal decomposition [43]. Phase field methods had proven to adequately describe such a process [8,34,35]. The phase field methodology can help to generate atomistic models of nanoporous metals with adequate control over the relative mass density and average ligament diameter, see Sun et al. [19] for a detailed application to the generation of an atomistic np-Au sample. When inspected under a transmission electron microscope, nanoporous gold foams exhibit two distinctive features, namely nanoscale grains [39,40] and filaments in the range of 10–100 nm [42,44]. Our first objective was to produce a computational sample with the same features.

In this paper, a nanoporous gold sample was generated from a bulk Au polycrystal. Fig. 1a shows a snapshot of the 3D polycrystalline Au bulk sample used for the generation of the foam. It was generated using Voronoi construction with random orientation angles to obtain random grain boundary orientations. Dimensions were $120 \times 120 \times 40$ nm^3. Aiming for an average grain size of 35 nm, the sample generation algorithm produced 16 grain centers as starting points for a regular fcc lattice with a parameter of 4.08 Angstrom and random orientations. Details of the algorithm can be found in [45]. The whole procedure resulted in a 16-grain periodic polycrystalline sample containing about 36 million Au atoms.

Separately we employed the phase field method to produce a structure template of two phases, *A* and *B*, using a simple fourth order polynomial double well free energy and an initial condition

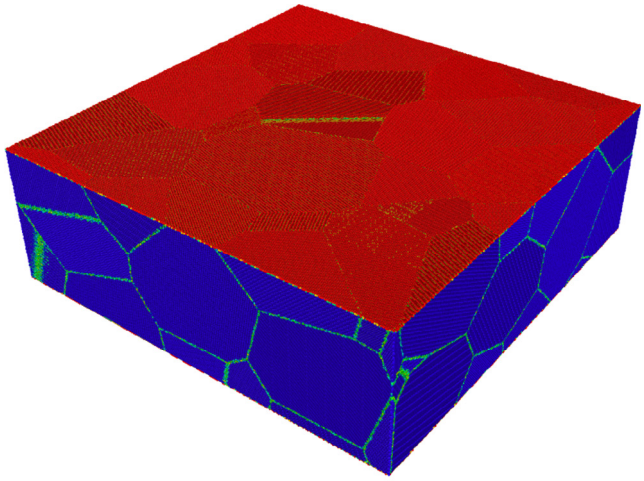

(a) Initial polycrystal

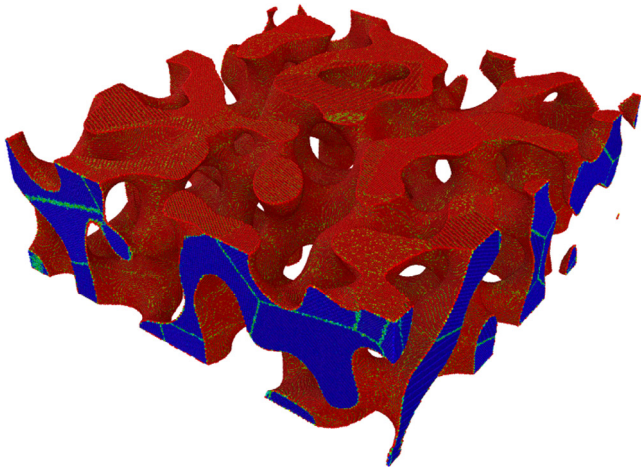

(b) Resulting foam

Fig. 1. (a) Perspective view of the initial polycrystal used for (b) the final foam generated. Red atoms indicate atoms in surfaces, blue correspond to atoms in perfect fcc positions and light-green indicate atoms in grain boundaries. (For interpretation of the references to color in this figure legend, the reader is referred to the web version of this article.)

of a randomly perturbed concentration within the spinodal region of the phase diagram. The system was evolved in time applying the Cahn–Hilliard equation using the MOOSE [46] finite element simulation framework until spinodal decomposition had proceeded to the desired length scale. The finite element solution was sampled at the atomic locations of the prepared polycrystalline sample and all atoms located in phase *A* – as determined by a threshold parameter – were removed to create pores, with the nanoscale porous structure resulting from the remaining phase *B* atoms.

Superposition of the Au atomistic sample and the phase-field template resulted in the polycrystalline Au nanofoam of Fig. 1b. The sample closely matches the nanoscale structure of nanoporous Au available in the experimental literature, see for example [47]. The resulting nanofoam had an Au polycrystalline structure of $120 \times 120 \times 40$ nm^3 with an average grain size of 35 nm, a relative density of 35 percent, with 12.7 million atoms. Employing an in-house code [48] following the suggestions of Sun et al. [19], we measured the ligaments and pores and statistically determined a mean pore diameter of 19.5 nm (with a standard deviation of 9.7 nm) and a mean ligament diameter of 11 nm (with a standard deviation of 7.5 nm).

Relaxation of the initially rigid and defect-free porous polycrystal in the absence of mechanical loading led to a sample with a number of dislocations, stacking faults and twin boundaries, in agreement with transmission electron micrographs of nanoporous Au produced by dealloying [47].

As a result of the whole procedure, we were able to generate, for the first time, an atomistic sample with pre-existing defects, that closely resembles np-Au foams produced by dealloying, combining nanoscale grains, ligaments and pores, with a high degree of realism. Our simulation box could be considered to be the representative volume element (RVE), containing 16 grains, and a volume whose dimensions are, on average, $10 \times 10 \times 4$ ligament diameters.

2.2. Simulation details

Our simulations were performed using LAMMPS [49]. The Au atomic interactions were modeled by means of an embedded atom model potential (EAM) [50]. Prior to indentation, the nanofoam was first minimized by the conjugate gradient method specifying a force tolerance of 10^{-8} eV/Angstrom and an energy tolerance of 10^{-6} eV as parameters for the satisfactory convergence of the minimization. Then the structure was thermally relaxed at 300 K for 6 ps using a NVE ensemble. Periodic boundary conditions were imposed in the x and y directions, perpendicular to the indentation axis. Three atomic layers at the bottom of the sample were imposed to be fixed, three additional layers were thermally controlled by means of a Langevin thermostat. Finally, the timestep was set to 3 fs.

We used a rigid hemispherical indenter interacting with the atoms in the target by a harmonic potential [51], $Vi = K(R - r_i)^2, R$ being the indenter radius, here taken to be 50 nm, and r_i the position of atom i, and with $K = 1000$ eV/nm^2 being the specified force constant. The indenter is frictionless, akin to a Hertzian indenter.

Indentation simulations were conducted in a displacement-controlled fashion by applying a constant penetration rate to the indenter [51,52]. A set of three penetration rates was inspected, namely 1, 10 and 100 m/s. These indentation speeds correspond to $\sim$3/10000 $C_0, \sim$ 3/1000 $C_0, \sim$ and 3/100 C_0 respectively, where C_0 is the directionally averaged sound velocity for Au. In this way, the effect of the penetration rate on the mechanical properties and plasticity mechanisms can be assessed. Indentation was carried on until a maximum penetration of 11 nm was reached.

The identification and tracking of defects was performed using the Crystal Analysis Tool [53]. Its output was visualized using OVITO [54].

3. Results and discussion

This section presents the results of the simulation and its post-processing, including load-penetration curves and hardness estimations (Section 3.1), the identification of deformation mechanisms (Section 3.2), extension of the plastic zone (Section 3.3) and a comparison with available scaling laws (Section 3.4).

3.1. Load – penetration behavior

Fig. 2a presents the load–displacement curves for our simulations. The curves for indentation speeds of 1 m/s and 10 m/s almost coincide. They begin with an elastic response up to a penetration of 2 nm after which a slight change in the load–displacement slope is perceived, corresponding to the development of plasticity in the region under the indenter. For a penetration rate of 100 m/s the elastic response appears stiffer up to a penetration of 1 nm, as expected due to the higher penetration rate. Again a change in the curve slope is a clear indication of the development of plasticity due to indentation.

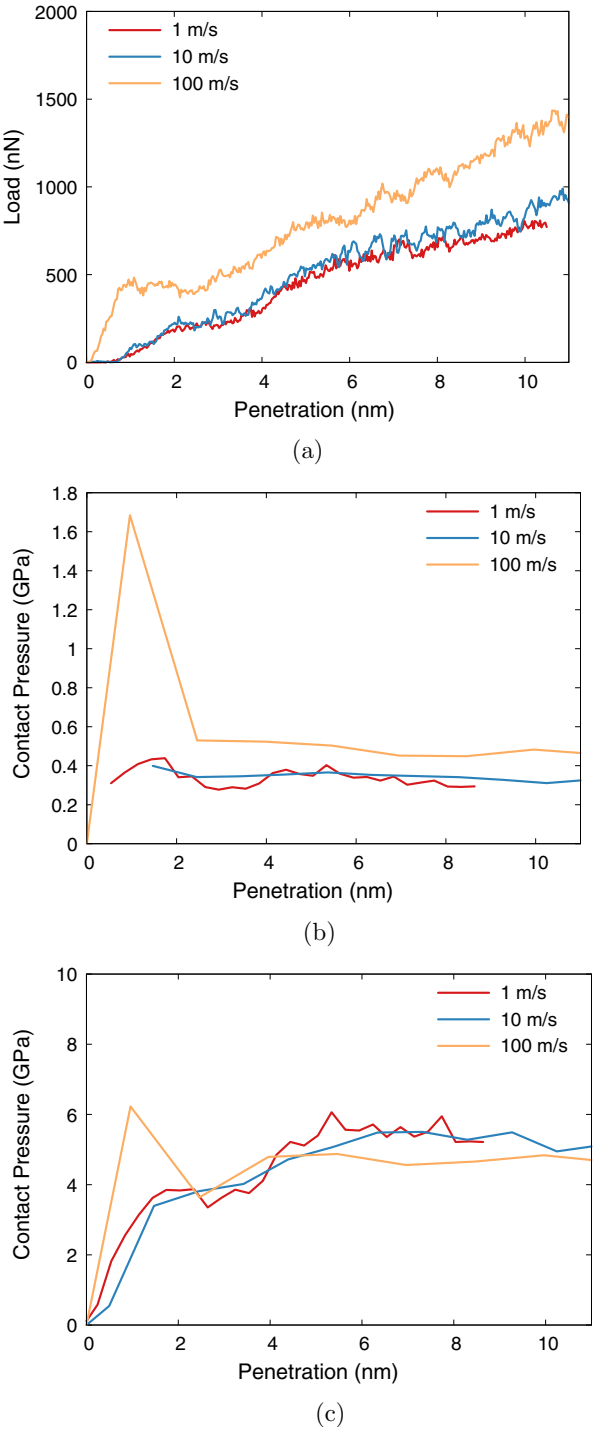

Fig. 2. (a) Load penetration curves. (b) Contact pressure evolution considering general bulk treatment and (c) atomistic treatment.

Sun and co-workers [55,56] studied the nanoporous gold thin films by in situ nanoindentation, coupling nanoindentation and transmission electron microscopy using penetration rates in the order of 1.5 to 30 nm/s. Their indentation curves present load drops that were correlated to compaction bursts of the foam. Our curves do not present marked load drops due to the considerably high penetration rates employed, note that our lowest penetration rate (1 m/s) is 10^8 times higher than the average penetration rate employed in Ref. [56].

Hodge, Biener and co-workers [14–16,31,41], performed extensive nanoindentation studies of nanoporous gold. Hodge et al. [31] employed a constant loading rate of 500 μN/s that based on their curves implies a penetration rate of 500–1200 nm/s. Their load displacement curves show a monotical increase in load with penetration, that is no load drops are seen, in contrast to Ref. [56]. Although our lowest penetration rate is about 10^6 times the ones used in [31], our loading curves share some features with those in Fig. 3 of Ref. [31] and Fig. 2 of Ref. [14] for 10 nm ligament size Au foams, i.e. the absence of marked load drops and load–displacement slopes in the range of 1–4 μN/nm.

The critical load to trigger plasticity increases as the penetration rate increases, as expected. A strain rate sensitivity exponent can be estimated using the stress at which plastic deformation is first noticeable (pop-in stress) divided by the ratio of strain rates, which we assume to be equal to the ratio of velocities:

$$m = \frac{\log \sigma_1/\sigma_2}{\log \dot{\epsilon_1}/\dot{\epsilon_2}} \tag{1}$$

By comparing the 100 m/s to 1 m/s cases, the estimation yields $m = 0.15$. This value, though high, is within the range and close to the upper bound of the values reported by Leitner et al. [57].

The hardness of the material is defined as the contact pressure that, once critical indentation depth has been exceed and a possible load drop has occured, stays rather constant with increasing indentation. In order to determine the attained contact pressures, the evolution of load has to be related to the contact area. For that purpose we will consider the projection of the convex contact surface onto the initial surface plane by using two very distinctive approaches, a traditional macroscopic one and an atomistic approach.

In a macroscopic level, the projected area can be computed based on the evolution of the diameter of the imprint. The contact pressure calculated with this conception is presented in Fig. 2b. The hardness considering the macroscopic approach is in the range of 300–400 MPa for the 1 m/s indentation rate, 350–380 MPa for the 10 m/s case and 450–550 MPa for the 100 m/s case. As a reference, the hardness values reported by Leitner et al. [57] for np-Au with relative density of 50 % and an average filament size of 100 nm are in the order of 400–700 MPa. Other studies report hardnesses in the range of 200–300 MPa for np-Au [16,14,31,58,33].

It must be pointed out that a direct comparison between the calculated macroscopic contact pressure and the hardness reported in experiments can only be made directly provided some conditions are met (i.e. similar indenter tip geometry, same ratio between contact area from the ligaments and overall contact area, similar contact area between the indenter and the nanoporous metal). As such a comparison is not possible due to lack of such information in the experimental references, the values cited above are provided only as a reference of the order of the magnitudes.

In an atomistic level, the contact area A^{atom} is the sum of the projected areas of all atoms i that become in contact with the indenter [59].

$$A^{atom} = \pi\beta^2 \sum_{i\,\epsilon\,contact} \cos\alpha_i, \tag{2}$$

where β is an atom radius and α_i is the angle formed by the indentation direction and the vector joining the center of the indenter with atom i. For Au we choose $\beta = 1.44$ Å. Fig. 2b presents the contact pressure–displacement curves considering the contact area through Eq. (2). The hardness considering the atomistic approach for contact area is in the range of 5–6 GPa for the 1 m/s indentation rate, 5–5.5 GPa for the 10 m/s case and 4.5–5 GPa for the 100 m/s case. These values, which are roughly an order of magnitude higher than those obtained by the macroscopic treatment, are of the order of magnitude of the yield strength of Au nanowires under tension [60,61].

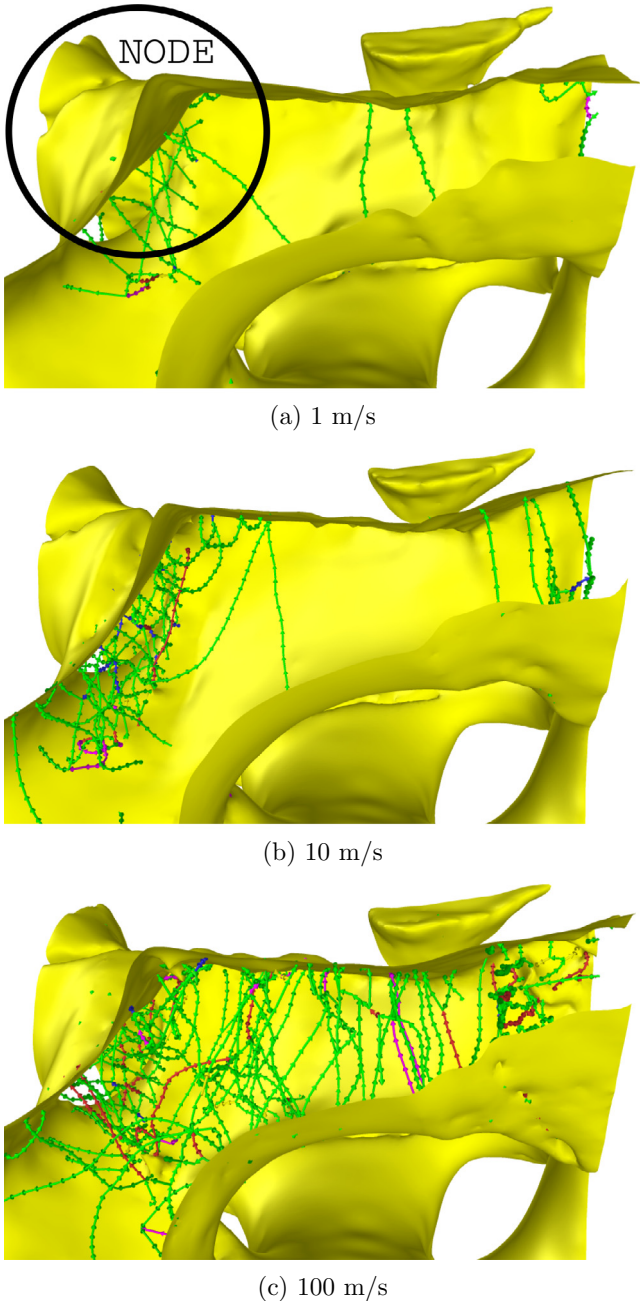

(a) 1 m/s

(b) 10 m/s

(c) 100 m/s

Fig. 3. Defective structures nucleated under the indenter for a penetration of 5.5 nm at different indentation speeds. Planar defects were intentionally removed for a clearer presentation of the dislocations. Foam surfaces are depicted in yellow. Lines indicate dislocations where blue: 1/2⟨110⟩ perfect dislocations, green: 1/6 ⟨112⟩ Shockley partials, pink: 1/6 ⟨110⟩ stair rod dislocations, yellow: 1/3 ⟨001⟩ Hirth partials, and red: double stair rod dislocations. (For interpretation of the references to color in this figure legend, the reader is referred to the web version of this article.)

Nanoindentation is a technique often used to infer mechanical properties of a material, yield strength being the most common. Since the technique does not test the mechanical properties of individual ligaments but senses the mechanical response of an ensemble of ligaments and pores, discrepancies often arise between yield strength measurements through tensile testing and those inferred from nanoindentation testing, as pointed out by Leitner et al. [57]. This is something expected considering

nanoindentation does not directly measure this property but relies on proportionality laws to derive the yield strength (σ) from the hardness measurements (H) based on a constant (C).

$$H \approx C\sigma \tag{3}$$

The determination of a proper hardness-to-yield-strength ratio (C), also known as the constraint factor, is not a trivial task since it varies with indenter type and mechanical properties of the material (i.e. Yield strength, Young's modulus, hardening index, Poisson's ratio) [62–65].

For sharp indenters probing fully dense solids, in which volume is conserved during plastic deformation, the constraint factor is in the range of 2.5–3.0 depending on friction and apex angle of the indenter tip [66], but also depends on properties of the material such as the Poisson ratio [65] and the yield-strength-to-elastic-modulus ratio [67]. For metallic foams, non-volume-conserving plasticity, the constraint factor is approximately in the range of 1.0 to $\left(1+2\frac{\rho_f}{\rho_s}\right)$ according to Ashby et al. [68], that is between 1.0 and 1.7 for our np sample with 0.35 relative density. For spherical indentation, C is a function of the indenter radius and the penetration achieved, but typically in the range of 1.0–1.5 approx. [69]. Regarding the relation between Poisson ratio and the constraint factor C, it is worth mentioning that a typical relation of hardness equal to three times the yield strength has the underlying assumption that the material has a Poisson's ratio of 0.5, while a one to one relation implies a Poisson's ratio of 0, a value assumed in some studies [16,31]. A value of 0.2–0.25 has been used for the treatment of nanoporous foams after the work of Balk and co-workers [32] and Volkert et al. [70]. Very recently, a work focused solely on the determination of the elastic and plastic Poisson's ratio of nanoporous gold [71], reporting that the elastic Poisson's ratio fluctuates in the range of 0.2–0.3 depending on densification but not on the ligament size. Based on the average ligament diameter of our simulations (11 nm) and the studies of Briot et al. [32] and Shaw and Sata [62], we will consider a Poisson ratio of the order of 0.2 which translates into a hardness-to-yield-strength ratio of 2.5. We will use this upper bound value of C so that each calculation of the yield strength derived from Eq. (3) results in a lower bound.

As a consequence of the application of Eq. (3) to the hardness computations performed above, the yield strength obtained from the atomistic treatment is in the range of 1.8–2.4 GPa, remarkably close to the yield strength of Au nanowires under tension [60,61]. Applying Eq. (3) to the hardness computations considering the macroscopic treatment renders a foam yield strength of 120–200 MPa. While the simulations presented here were performed at the same indentation point, we expect no differences in the properties should the indentation be performed in a different place given that they are extracted after achieving a significant penetration that guarantees contact with several ligaments, as shown in Section 3.3.

Recently, Kim et al. [72] studied the indentation size effect (ISE) in nanoporous gold on samples with ligament size 26 nm and above, finding that the ISE for np-Au depends on ligament size. No ISE was verified in the present work, whether this can be attributed to the smaller ligament size used in this work or other simulation conditions is yet to be determined and is left for a future work.

3.2. Deformation mechanisms

Shockley partials and Lomer-Cottrel locks [73] appear to be the main defects involved in the plastic deformation of the nanoporous gold under tension [19] and compression [21,37].

In our nanoindentation simulations, three different deformation mechanisms were identified, namely dislocation activity, twinning and grain boundary sliding.

Dislocation activity is the main deformation mechanism. We were able to identify Shockley partials originating at the ligament surfaces and also at grain boundaries. Fig. 3 presents details of the defective structures for a single ligament under the indenter for a penetration of 5.5 nm. Fig. 3a corresponds to a penetration rate of 1 m/s and shows a few Shockley partials ($\vec{b} = 1/6a[\bar{1}\,\bar{2}\,1]$), depicted in green. Shown in pink, a couple of Lomer-Cottrel dislocation locks can be spotted. This is a sessile dislocation that can appear after the reaction of two Shockley partials and, by impeding slip in $(1\,1\,1)$ planes, it behaves as a barrier for the movement of additional dislocations, contributing to strain hardening. Plasticity is concentrated at the nodes of the foam.

For a penetration of 10 m/s, Fig. 3b not only shows a larger number of Shockley partials and some Lomer-Cottrel locks but also a few perfect dislocations ($\vec{b} = 1/2a[1\,1\,0]$), depicted in blue.

For the highest penetration rate, Fig. 3c shows a vast amount of Shockley partials, together with long segments of Lomer-Cottrel locks and some perfect dislocations. A few Hirth sessile dislocations ($\vec{b} = 1/3a[0\,0\,1]$), depicted in yellow, were also found in a small amount. The presence of long Lomer-Cottrel locks and Hirth dislocations can also play their part in the higher contact pressures obtained for the 100 m/s case due to their contribution to strain hardening.

Red segments can be seen in each panel of Fig. 3, they correspond to dislocations not identified by the algorithm employed for classification. Detailed analysis revealed that they are double stair-rod dislocations with $\vec{b} = 1/6a[0\,2\,2]$ [21,74].

Fig. 4 presents the evolution of defects for two sections of the sample indented at 1 m/s. Fig. 4c shows the first defects nucleated for a depth of 4.7 nm. The interaction of two partials can be appreciated. As penetration reaches 7.2 nm, triple, and quad stacking faults are found. For a penetration of 9.5 nm the density of planar defects is considerably high. The filaments are now vastly populated by intrinsic, triple and quad stacking faults. Detailed inspection shows the nucleation of dislocations on free surfaces and on grain boundaries, the former being predominant over the latter. In relation to source limited plasticity, Fujita et al. [75] transmission electron microscopy studies had shown that the curved surfaces of nanoporous gold have a high density of atomic steps and kinks and then Farkas et al. [18] small scale simulations suggested that these steps have an important role in plastic deformation providing sites for dislocation emission. This is verified in our results. Dislocations move through the filament until they reach a free surface, where they annihilate leaving stacking faults behind. The constrained motion of dislocations along the ligaments reported by Viswanath et al. [26] and attributed to a concentration of vacancies was not confirmed in our study, possibly due to the lack of a significant amount of vacancies. No significant trapping of dislocations at the grain boundaries was verified.

It is worth noting that the deformation behavior of nanoscale objects [e.g. nanoscale pillars] is often discussed in terms of dislocation starvation models [76], where mobile dislocations propagate through the material and annihilate when they reach a free surface. In contrast to this scenario, our simulations show the presence of several dislocations within ligaments (Fig. 3) together with a large increase in dislocation count (see Section 3.3) clearly pointing out to a dislocation accumulation scenario. Our analysis also reveals several sessile dislocations which are a the result of dislocation interaction (Fig. 3). These observations imply that a dislocation-starvation scenario does not apply for nanoporous gold, a similar conclusion drawn in previous MD studies [37]. A dislocation accumulation scenario has already been observed by transmission electron microscopy in the contributions by Dou and Derby [77,47].

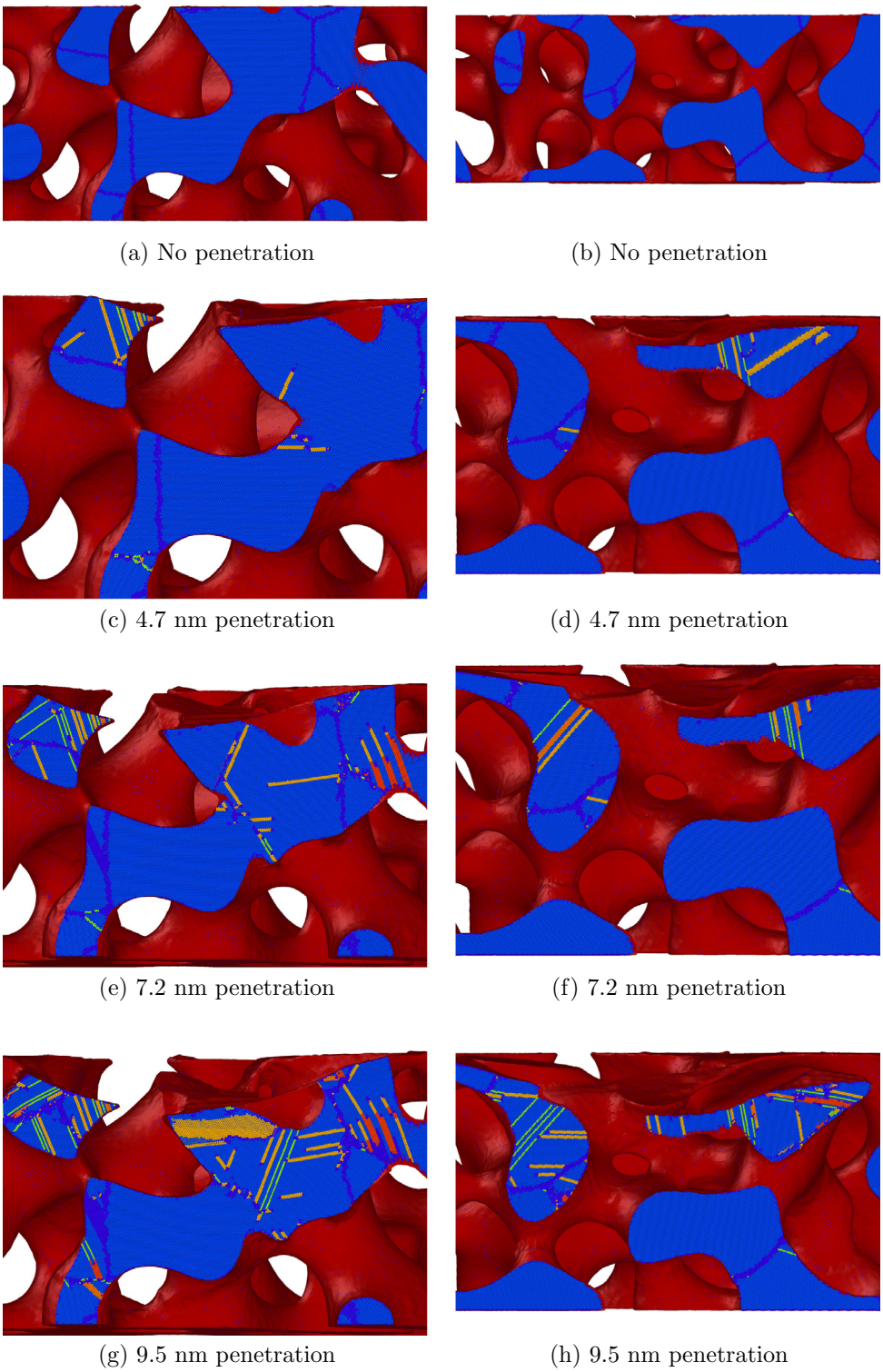

(a) No penetration (b) No penetration

(c) 4.7 nm penetration (d) 4.7 nm penetration

(e) 7.2 nm penetration (f) 7.2 nm penetration

(g) 9.5 nm penetration (h) 9.5 nm penetration

Fig. 4. Evolution of the atomic structure under the indenter for a penetration rate of 1 m/s. Right hand side and left hand side columns correspond to two perpendicular cuts of the sample. Foam surfaces are depicted in red. Blue atoms correspond to perfect fcc atoms, light-green atoms (in single layer arrangements) correspond to coherent twin boundaries, light-orange atoms (in dual layer arrangements) correspond to intrinsic stacking-faults, dark-orange atoms (in triple layer arrangements) pertain to triple stacking faults while red ones (in four layer arrangements) belong to quad stacking faults. (For interpretation of the references to color in this figure legend, the reader is referred to the web version of this article.)

Twinning was also identified. Twin boundaries are shown in Fig. 4 with light-green. The quantification of atoms in twin boundaries reveals that twinning starts and increases with indenter penetration. The fraction of atoms in twin boundaries is lower than that of intrinsic stacking faults and it gets lower as the indenter speed rises, as shown by Fig. 5a–c.

Displacement vector analysis performed with OVITO reveals the occurrence of grain boundary sliding. Fig. 6 shows an inset of two grains separated by a grain boundary where fcc atoms are depicted in dark blue while grain boundary atoms are shown in light blue. The orientation of the grain boundary is almost parallel to the loading axis. Calculated displacement vectors are shown by yellow

arrows. Differences in length of the arrows on each side of the GB distinctively show sliding, the difference accounts for 2–4 Å.

3.3. Extension of the plastic zone

Proper identification and tracking of the evolution of defects and displacements allows for the determination of the extension of the plastic zone.

Fig. 7 presents results of the computation of atomic displacements for a penetration of 8.4 nm achieved at 1 m/s (Fig. 7a, c) and 100 m/s (Fig. 7b, d) indentation rates. Blue color corresponds to atoms who had experienced a displacement $\geqslant 2a_0 = 8.16$ Å, while red color corresponds to atoms directly in contact with the indenter. It can be seen that the several ligaments are probed by the indenter. This image is a qualitative indication of the volume of the material that is influenced by the indenter and the relation between the contact area from the ligaments, the total contact area and the material volume probed. It shows that, for a given penetration, the contact is greater for the higher indentation rate, due to a larger deformation of the ligaments in contact with the indenter for the 100 m/s case, and that the propagation of the imposed displacement diminishes as the indentation rate increases. In other words, deformation appears to be more localized as the penetration rate increases.

The extension of the plastic zone can be quantitatively determined. Fig. 8 presents the outcome of a Common-Neighbor-Analysis [78] performed in OVITO for the undeformed sample (Fig. 8a, b), and for a penetration of 8.4 nm achieved at 1 m/s (Fig. 8c, d) and 100 m/s (Fig. 8e, f) indentation rates. Atoms in perfect fcc position are not shown. Red color corresponds to atoms in hcp position, that belong mainly to fcc stacking faults but also to some grain boundaries. Blue color corresponds to atoms in bcc position. Fig. 8a and b reveal a low amount of defects in the undeformed sample. For the 8.4 nm penetration and regardless of the indentation rate (Fig. 8c–f), it can be seen qualitatively that the extension of the planar defects is similar to the extension of the blue zone depicted in Fig. 7 for each indentation rate, confirming the conclusion about the localization of deformation and plasticity.

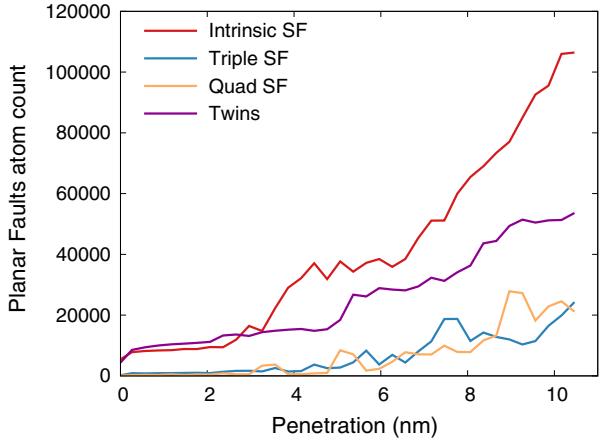

(a) 1 m/s.

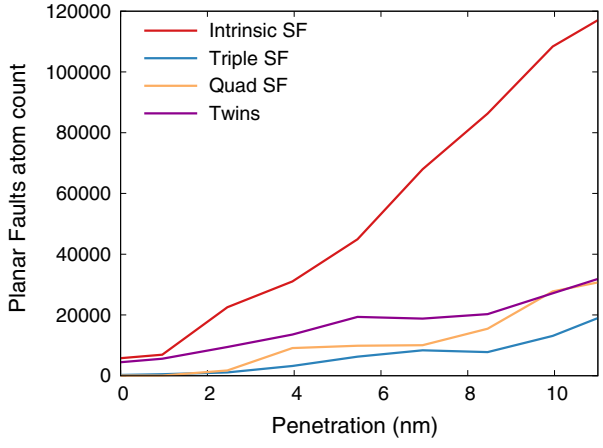

(b) 100 m/s.

Fig. 5. Evolution of the atom count for planar defects.

Beginning from the moment that the indenter makes contact with the surface and until the largest penetration is achieved, the atomic configurations are also analyzed by means of the dislocation extraction algorithm (DXA) [53,79]. From these analyses the conguration of the dislocation lines are obtained. The criteria used in this research was to compute and track the total length of Shockley partials by means of an in-house code which defines hemispherical shells and computes the total dislocation length in each shell, see the work of Hua and Hartmaier [80] for conceptual details and that of Gao et al. [81] for an application example; the shell thickness was chosen as 2 nm. The result is a radial profile of the Shockley partials distribution during nanoindentation. The plots in Fig. 9 present the results of the calculations; as the indenter touches the foam and plasticity develops, the count of Shockley partials length significantly increases from the initial distribution to a non uniform distribution with a few peaks as the indenter further penetrates into the target, each peak corresponding to the concentration of partials within each ligament. Based on Figs. 8 and 9, the plastic zone extends for about 20–25 nm around the indent. For an 8.4 nm penetration, radius of the imprint is 28 nm, hence the plastic zone extends for about 1.7–1.9 times the radius of the imprint. This is significantly lower than the values for bulk fcc metals reported by Gao et al. [81], suggesting that np foams are effective materials for the confinement of plasticity in cases of dynamic indentation. The case of extreme indentation velocities of km/s could be considered from cluster impact simulations by Anders et al. [82], who found extensive plastic zones, as large as for compact targets, in their simulations.

Inspired by the work of Sun et al. [19], an automated pore and filament measurement algorithm was implemented, its details to be presented elsewhere [48], and the results are shown in Fig. 10. The calculations indicate that for a given penetration, no significant differences are found in the pore size distribution for two different indentation rates, and that as penetration increases, the distribution of measurements shows a reduction of the pore diameter, without noticeable reduction of the ligament size.

3.4. Scaling laws

Applications of nanofoams, such as those mentioned in the Introduction, impose a manufacturing challenge since the tailoring of ligament and pore sizes have an impact on the mechanical properties of the foam and an adequate correlation of dimensions, mechanical properties and deformation mechanisms at the nanoscale is still lacking. The purpose of this section is to revisit several well-established scaling laws and compare their predictions with the yield strength estimations derived in Section 3.1. We discuss on some of the assumptions of each model and possible reasons where discrepancies are found.

At the macroscale, the main deformation mechanisms of open cell foams under compression are elastic buckling and plastic collapse. An example of the former can be found in the contributions of Feng and co-workers [83], who studied the effects of surface energy and residual surface stress on the effective elastic properties of nanoporous materials and, as a result, they presented mod-

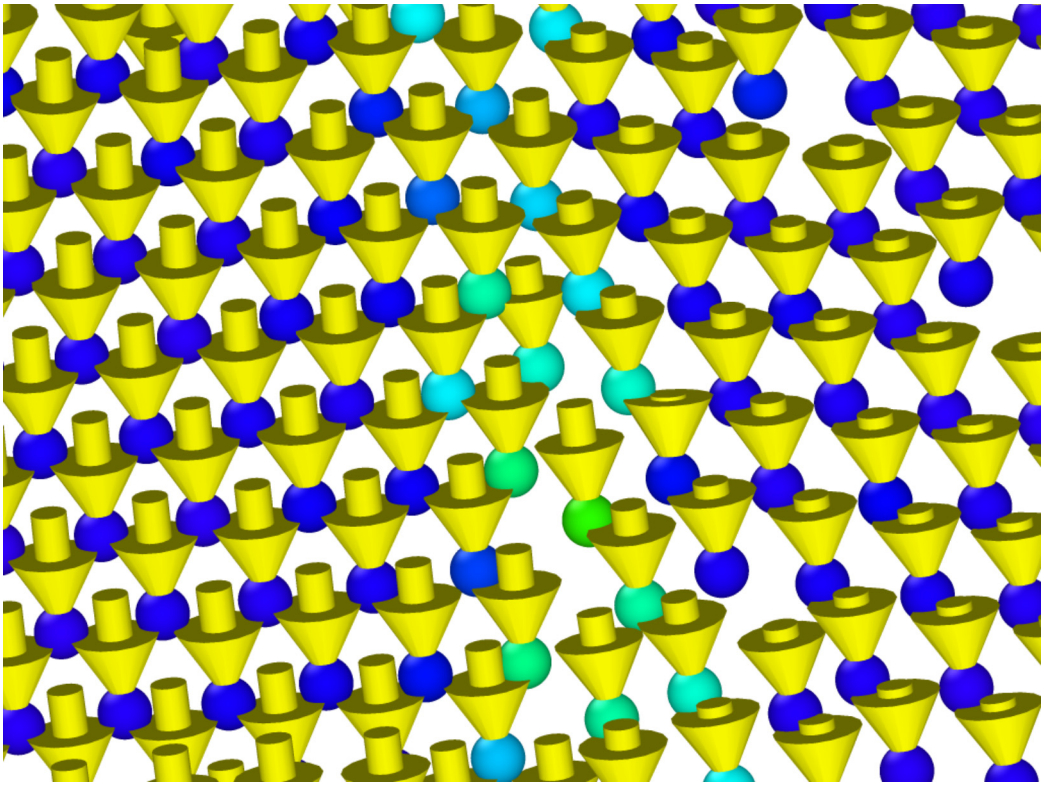

Fig. 6. Detailed view of two grains separated by a grain boundary (GB atoms depicted in light-blue). Loading axis is almost parallel to the orientation of the grain boundary. Displacement vectors are shown in yellow. Differences in length of the arrows on each side of the GB distinctively show GB sliding. (For interpretation of the references to color in this figure legend, the reader is referred to the web version of this article.)

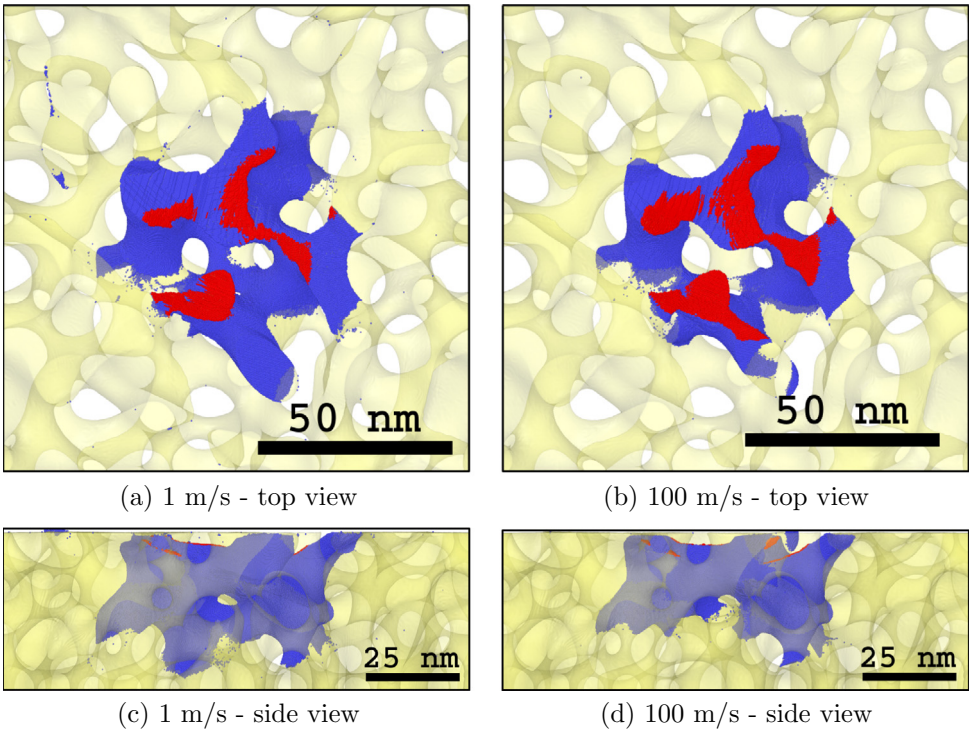

(a) 1 m/s - top view (b) 100 m/s - top view

(c) 1 m/s - side view (d) 100 m/s - side view

Fig. 7. Atomic displacements for a penetration of 8.4 nm. Red atoms are those directly in contact with the indenter. Blue atoms correspond to particles displaced at least 2 a_0. Deformation gets more localized as the penetration rate increases. (For interpretation of the references to color in this figure legend, the reader is referred to the web version of this article.)

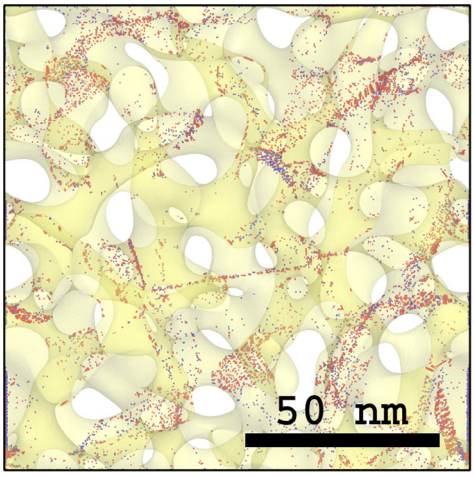

(a) Undeformed sample - top view

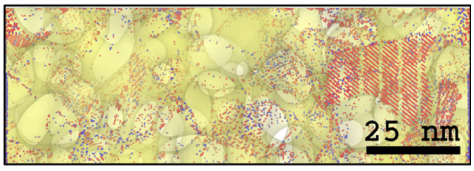

(b) Undeformed sample - side view

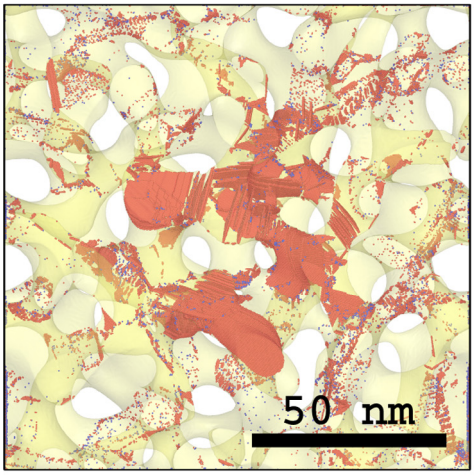

(c) 1 m/s - top view

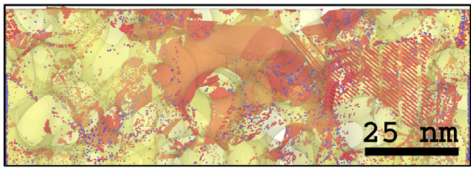

(d) 1 m/s - side view

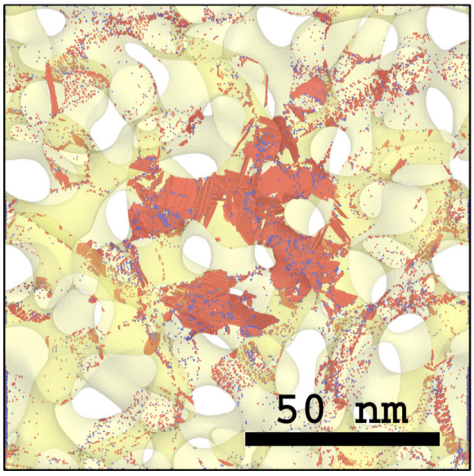

(e) 100 m/s - top view

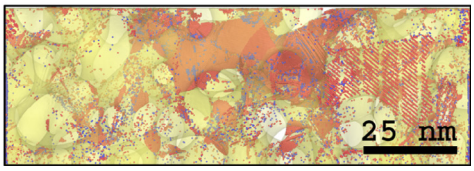

(f) 100 m/s - side view

Fig. 8. Non-fcc atoms for the undeformed sample and for a penetration of 8.4 nm at two different indentation rates. Red atoms correspond to hcp structures and blue ones to bcc structures. The extension of the stacking faults is a unique indication of the extension of the plastic zone. (For interpretation of the references to color in this figure legend, the reader is referred to the web version of this article.)

ified Euler–Bernoulli and Timoshenko beam models [84]. A paradigmatic example of plastic collapse models is that of Gibson and Ashby [30], which considers that deformation is controlled by plastic hinges at the rigid nodes and was originally derived as a model for porous materials with macroscopic porosity, in which the yield strength of the porous material can be estimated based on that of the corresponding fully dense material through

$$\sigma^* = C^* \cdot \sigma_s \cdot \left(\frac{\rho^*}{\rho_s}\right)^n \tag{4}$$

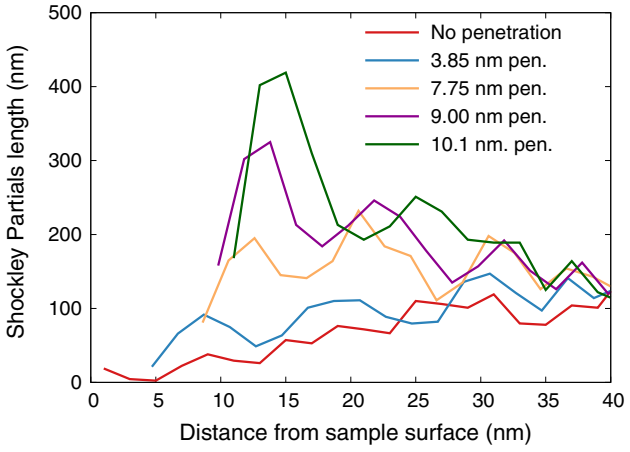

(a) 1 m/s.

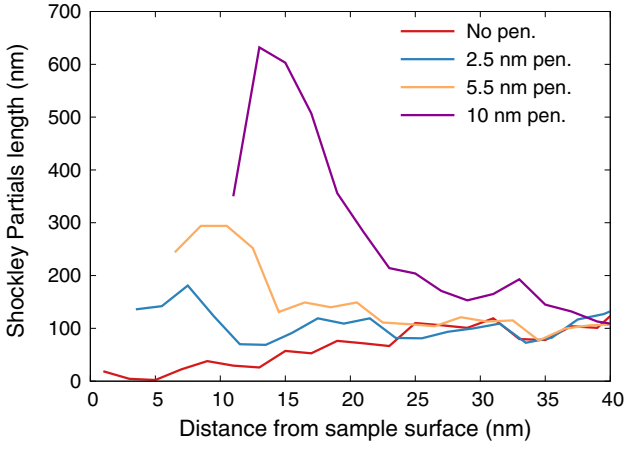

(b) 100 m/s.

Fig. 9. Evolution of the plasticity profile represented by the total length of Shockley partials.

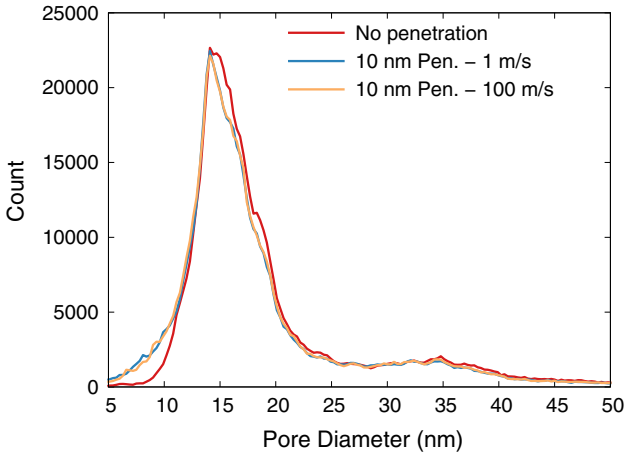

(a) Pore size histogram.

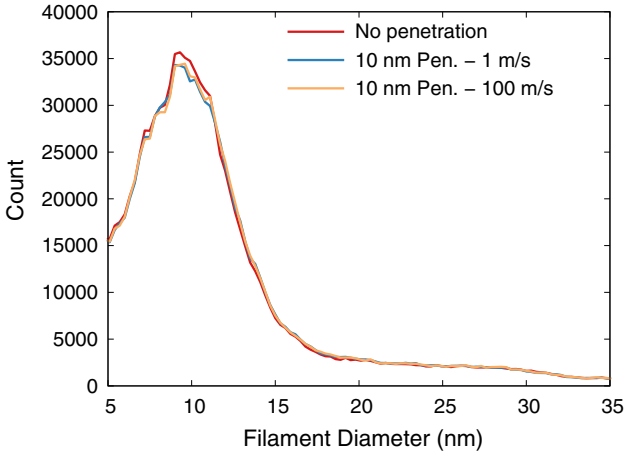

(b) Filament size histogram.

Fig. 10. Histograms of cord length measurements for a penetration of 10 nm show the closure of pores without noticeable change in the ligament diameter.

with $n = \frac{3}{2}, C^* = 0.3$ and σ^* and σ_s the yield strengths of the porous material and the corresponding ligament material in bulk form, respectively, ρ^* the foam density and ρ_s the bulk material density.

Application of Eq. (4) to the bulk values by Sakai et al. [85] for a 36 nm grain size Au sample renders a yield strength of 18.6 MPa, an order of magnitude smaller than the estimations of Eq. (3) (120–200 MPa) but similar to the values by Balk et al. [86] for their tensile and compressive tests of micron sized samples of bulk nanoporous gold. Chung Cheng and Hodge [87] suggested using the yield strength of the ligament as σ_s in Eq. (4), and based on our estimations in Section 3.1 (1.8–2.4 GPa) renders 110 MPa $\leqslant \sigma^* \leqslant$ 150 MPa, a yield strength that is significantly higher than the ones obtained by Balk et al. for their tensile tests [86]. This can obey to the well known strain rate effect in MD simulations or might be an indication that Eq. (4) is not applicable to a np-Au foam as the one studied here. Other experimental and computational studies pose concerns on the use of the standard G-A equation on nanoporous foams [33,31,18,19,88]. For instance, Biener et al. [14] used the standard G-A equation on their np-Au nanoindentation study (0.25 relative density, 10 nm ligament dia.) and obtained a predicted ligament yield strength of 4.5 GPa, which is far greater than the 1.1 GPa value obtained by Lu et al. [89] when testing 10 nm diameter wires under tension. Nanoporous foams are a distinctive type of material where not only grain size is at the limit of a Hall–Petch/Inverse Hall–Petch behavior but also ligaments are so thin that surface effects can play an important role, producing a significant deviation from the expected behavior of the typical beam-under-bending model used for the derivation of scaling laws. As a consequence, the validity of Eq. (4) is still under debate.

Let us compare yield strength obtained in Section 3.1 with values predicted using scaling laws available in the literature.

Inspired by the Hall–Petch relation, Hodge et al. [31] modified the G-A scaling law by adding a term accounting for the effect of the ligament size. As a result they presented the following scaling equation:

$$\sigma^* = C_s\left[\sigma_s + k \cdot L^{-1/2}\right] \cdot \left(\frac{\rho^*}{\rho_s}\right)^{3/2} \tag{5}$$

where C_s is a fitting coefficient typically taken as 0.3 [30], σ_s is the bulk material yield strength, k is a Hall–Petch-type coefficient for the theoretical yield strength of Au in the corresponding size regime, L is the ligament size. $\sigma_s + k \cdot L^{-1/2}$ is termed the ligament yield strength, and by considering $\sigma_s = 200$ MPa, $k = 9200$ MPa $\cdot$ nm$^{1/2}$ after [85] and $L = 11$ nm, its calculation renders 2.9 GPa, 20 % above the upper bound of the range of the ligament yield strength values estimated in Section 3.1 (1.8–2.4 GPa). Using Eq. (5) for the simulated foam renders a calculated yield strength of 180 MPa.

To account for the effect of plastic strain gradients that exist in the deformation hinges of the typical foam model with beams and

nodes, Dou and Derby [77] presented a modified plastic collapse model for nanoporous foams where the yield strength of the ligament is:

$$\sigma_Y = \sigma_1 + k_3 \mu \sqrt{\frac{b}{t}} \tag{6}$$

where σ_1 is the yield stress of the ligament in the absence of strain gradients, k_3 incorporates Taylor's constant and all geometrical or shape terms related to the ligaments in the structure, μ is the shear modulus, b is the Burgers vector and t is the ligament width. Following the suggestion of Chung Cheng and Hodge [87], one could use the derived yield strength σ_Y and introduce it into σ_s of the standard Gibson and Ashby equation, obtaining the yield strength of the foam. So the use of Eq. (6) renders a ligament yield strength of 2.7 GPa, where the parameters of the equation were taken as $\sigma_1 = 1$ GPa, $b = 0.288$ nm, $t = 11$ nm, $\mu = 30$ GPa, and $k_3 = 0.47$ after Dou and Derby [77]. Then introducing $\sigma_s = 3.2$ GPa on Eq. (4) renders a foam yield strength of 198 MPa.

To account for the effect of capillary forces on the mechanical properties of np-Au, Farkas and co-workers [18] presented a tension/compression asymmetry model of the form

$$\sigma^*(d) = \sigma_{HP}(d) + \sigma_s(d) \tag{7}$$

where the first term aims to capture a Hall–Petch type behavior without the effect of the surface stress

$$\sigma_{HP}(d) = \begin{cases} \frac{\alpha}{d^{1/2}} & d > 20\ \text{nm} \\ \frac{\alpha}{20^{1/2}} & d < 20\ \text{nm} \end{cases} \tag{8}$$

while the second term is added to account for the contribution of surface stress

$$\sigma_s(d) = \begin{cases} -\frac{\beta\gamma}{d} & compression \\ +\frac{\beta\gamma}{d} & tension \end{cases} \tag{9}$$

with γ being the surface tension and α and β constant fitting parameters. For their tension/compression study, Farkas et al. determined $\gamma = 1.9$ GPa, $\alpha = 420$ MPa nm$^{1/2}$, and $\beta = 135$. Considering our average ligament diameter, the use of Eqs. (7)–(9) render $\sigma_{HP} = 94$ MPa and values of σ^* in the range of 118 MPa (tension) to 70 MPa (compression).

Recently, Briot and Balk [33] proposed a scaling relation for the yield strength of nanoporous metals as:

$$\sigma^* = Ck l^{-m} \left(\frac{\rho^*}{\rho_s}\right)^n \tag{10}$$

where σ^* is the foam yield strength, C is a fitting coefficient, k is a size effect coefficient, l is the ligament size, m is the size effect exponent, n is the scaling effect exponent due to the porous structure, ρ^* the foam density and ρ_s the bulk material density. Based on their nanoindentation study, the authors updated the expresion to describe the yield strength of np-Au as a function of relative density and ligament diameter:

$$\sigma^* = 1.939\sigma_s \left(\frac{\rho^*}{\rho_s}\right)^{2.618} \quad with\ \ \sigma_s = 0.0328\ \text{MPa} \cdot \text{l}^{-0.551} \tag{11}$$

where σ_s is the yield strength of the ligament in bulk form. The use of Eq. (11) predicts a foam yield strength of 99 MPa by considering $\sigma_s = 796$ MPa as a result of the 11 nm ligament size.

The foam yield stress results of Eqs. (3), (5)–(7) and (11) are condensed in Table 1 for comparison purposes. The results of Eqs. (5) and (6) fall within the range estimated through Eq. (3) (120–200 MPa).

The standard Gibson and Ashby equation (Eq. (4)) tends to be left aside when studying the mechanical properties of np metals due to the fact that the expression lacks of any size effect terms

Table 1
Summary of ligament and foam yield strengths computed from relationships in the literature.

	σ_Y(GPa)	σ^*(MPa)
Eq. (3)	N/A	120–200
Eq. (5)	2.9	180
Eq. (6)	3.2	198
Eq. (7)	N/A	70–118
Eq. (11)	0.79	99

(both for ligament size and grain size), it does not take into account strain gradient plasticity, etc. Nevertheless, there is a general agreement that except for high density nanoporous metals, nanofoams tend to deform in a way typically dominated by beam bending with plastic collapse at the nodes or close to them, consistent with the concept that Gibson and Ashby developed and, as a result, many scaling laws for np metals are derived from or inspired by the G-A model. Eqs. (5) and (6) are two such cases, where the former considers both ligament size effects and grain size effects through the term $k \cdot L^{-1/2}$. In the latter, Dou and Derby [47] considered strain gradient plasticity by means of the concept of geometrically necessary dislocations and a Taylor hardening expression, and also considered dimensional aspects of the foam, namely the filament size. In an attempt to consider size effect strengthening and axial contributions to the deformation modes, Briot et al. [33] presented Eq. (11), which seems akin to the previous ones but differs in the election of the coefficients. The equation was fitted to the outcome of tensile tests. From such tests [32], the yield strength proved relative low, most probably testing the foam flaws rather than the ligament strength and as a result, our calculations using Eq. (11) rendered a lower value for our foam, which we attribute to a possible underestimation of the ligament yield strength, since nanoscale tests of Au wires had shown a yield strength of 1 GPa and above. It must be pointed out that the np-Au samples tested in [32,33] have a grain size much larger than the filament size, about three orders of magnitude, this condition being a major difference with the np-Au sample used in this work.

The nanoporous foam probed in this paper exhibits a grain size that is close to the limit of a Hall–Petch/Inverse Hall–Petch behavior, with ligaments within the same order of magnitude. Plasticity tends to concentrate at the nodes, supporting the hypothesis made in models derived from the Gibson Ashby scaling law regarding the location of plasticity. In particular, plasticity occurs in the form of dislocations, verifying the assumption made by Dou and Derby in their model [77]. Of all the scaling laws tested, the one by Hodge and co-workers [31] seems to be the most suitable since it was obtained after nanoindentation testing and takes into consideration nanoscale effects both, for the ligament size and for the grain size of the foam. The yield stress derived from Eqs. (5) and (6) is in remarkable agreement with the foam yield stress estimation of Eq. (3), further supporting the election of the hardness-to-yield-strength ratio made in Section 3.1. Of the models akin to G-A, the model by Briot and Balk [33] renders the lowest values, probably due to a low value of ligament yield strength. Our results suggest that the latter should be updated to that of Au nanowires. Although no single model takes into account all the physical aspects revealed in our study, it is fair to conclude that the ligament size and the ligament yield stress seem to be the dominating factors on the mechanical properties obtained here.

As a consequence of the high surface-to-volume ratio of nanoporous materials, capillary forces can also affect the strength, which led Farkas and co-workers [18] to propose a model with a Hall–Petch type term and a term due to surface stresses. Its application to the sample of this research renders a lower bound for the foam yield stress, see Table 1. However, the model has three con-

stants that might need to be adjusted for its use, namely α, β and γ. Constants β and γ are related to the surface stress and modulate the tension/compression asymmetry. In our case, we followed the atomic stress calculation done in Ref. [18], obtaining surface stresses of the order of 2 GPa, in agreement with the last reference. Therefore, we consider $\beta = 135$ and $\gamma = 1.9$ GPa as adequate constants for our sample. In turn, α has a direct role on the adjustment of the average of σ^* and might be the main reason for the low stress derived from the model by using $\alpha = 420$ MPa nm$^{1/2}$. For instance, should we choose $\alpha = 800$ MPa nm$^{1/2}$, we would obtain σ^* in the range of 202 MPa (tension) to 154 MPa (compression), in better agreement with the results of Eqs. (5) and (6). Its quotient is also in agreement with the tension/compression ratio presented by Farkas et al. in their Fig. 7 [18]. Further tension and compression studies are required to properly determine the adequate value of the constants involved in the model for a given np-Au sample.

In a very recent contribution, Mangipudi Epler and Volkert [29] studied the effects of structural topology on the mechanical properties of nanoporous gold and presented modified scaling laws to account for these effects. They show a linear dependence of the geometric pre-factors of Gibson and Ashby scaling laws with the scaled genus density. There are signs that topological and morphological concepts, such as network connectivity [27], scaled genus density [29], and mean principal curvature [90,91] can help to adjust scaling laws for their use at the nanoscale [92]. A thorough topological characterization of the nanoporous sample used in the current study is out of the scope of this work and therefore a comparison with topologically-based models (e.g. network connectivity models) is left for a future work.

All in all, the debate on the validity of Gibson-Ashby equations will continue, where it can be foreseen that a systematic experimental and computational joint study is mandatory, involving a great number of experiments and MD simulations of Au single crystalline foam, and similar foams as in the present investigation with a variety of grain size and ligament size.

4. Conclusions

We study the mechanical response of nanoporous Au under nanoindentation by means of atomistic simulations of a computational domain that mimics the complex structure of Au foams produced by dealloying. We compute the contact pressures, we analyze the deformation mechanisms and we test a variety of scaling laws. Our findings are in agreement with experimental nanoindentation studies of np gold [14,16,31,55–57]. The main conclusions are:

- Load penetration curves share features with their experimental counterparts available in the literature.
- Deformation occurs by dislocation accumulation. Plasticity is dominated by dislocation nucleation on free surfaces and their propagation across the ligament. As a number of dislocations reach another surface they annihilate, leaving behind a significant number of intrinsic stacking faults. Dislocations are mainly of the Shockley partials type, but perfect dislocations, Hirth partials and Lomer-Cottrel locks were also identified. The occurrence of mechanical twinning and grain boundary sliding was verified.
- Plasticity develops mainly at the nodes of the foam and it is confined to a region in the vicinity of the indenter, whose thickness is 1.7–1.9 times the radius of the imprint, as verified by hemispherical quantification of Shockley partials, extension of stacking faults and displacement calculations. The extension of the plastic zone is smaller than in the case of bulk fcc metals under nanoindentation. The histograms of cord length measurements indicate that the closure of pores occurs without noticeable change in the ligament diameter.
- The foam yield strength derived from the hardness computation shows good agreement with estimations obtained using a variety of scaling laws. This is an indication that the constraint factor chosen in this study is a good measure of the hardness-to-yield-strength ratio for np-Au.

Finally, while the details we have discussed specifically apply to spherical nanoindentation of Au nanofoams, the general features can probably be generalized to other fcc nanofoams of technological interest (Ag, Pd and Cu) where plastic collapse appears to be the dominant mechanism [87]. Future work in the field should include similar studies of other nanofoams of technological interest in bcc metals. This work provides links to close gaps between continuum-scale models, atomistic models and experiments. Np Au with ligament sizes under 20 nm suffer from high surface-induced stresses [18], and in such cases, it has been shown that linear elastic FEM models yield higher stiffnesses than MD simulations thanks to the nonlinear elastic behavior of the EAM potential used in the latter [36]. In a similar way, this work can be a useful benchmark for FEM models of np-Au subjected to spherical indentation. Also, analysis of the extension and shape of the plastic zone from MD simulations could be coupled with experiments such as focused ion beam aided characterization of nanoindents in np Au [93], aiming for further insights into the deformation behavior of np structures.

Acknowledgments

CJR thanks funding from PICT-2015-0342, a SeCTyP UNCuyo grant, and HPC computing resources at Lawrence Livermore National Laboratory and Mendieta CCAD-UNC through PDC-SNCAD MinCyT innitiative. EMB thanks funding from PICT-2014-0696 and a SeCTyP UNCuyo grant. ENM thanks support by SeCTyP UNCuyo. The Tesla Titan X Pascal used for this research was donated by the NVIDIA Corporation. The authors thank the anonymous reviewers for their valuable comments.

References

[1] M.A. Meyers, P.-Y. Chen, A.Y.-M. Lin, Y. Seki, Biological materials: structure and mechanical properties, Prog. Mater Sci. 53 (1) (2008) 1–206.
[2] P.-Y. Chen, J. McKittrick, M.A. Meyers, Biological materials: functional adaptations and bioinspired designs, Prog. Mater Sci. 57 (8) (2012) 1492–1704.
[3] Y. Ding, M. Chen, J. Erlebacher, Metallic mesoporous nanocomposites for electrocatalysis, J. Am. Chem. Soc. 126 (22) (2004) 6876–6877.
[4] J. Snyder, T. Fujita, M. Chen, J. Erlebacher, Oxygen reduction in nanoporous metal–ionic liquid composite electrocatalysts, Nature Mater. 9 (11) (2010) 904–907.
[5] A. Wittstock, V. Zielasek, J. Biener, C. Friend, M. Bäumer, Nanoporous gold catalysts for selective gas-phase oxidative coupling of methanol at low temperature, Science 327 (5963) (2010) 319–322.
[6] J. Erlebacher, M.J. Aziz, A. Karma, N. Dimitrov, K. Sieradzki, Evolution of nanoporosity in dealloying, Nature 410 (6827) (2001) 450–453.
[7] D. Kramer, R.N. Viswanath, J. Weissmüller, Surface-stress induced macroscopic bending of nanoporous gold cantilevers, Nano Lett. 4 (5) (2004) 793–796.
[8] J. Biener, A. Wittstock, L. Zepeda-Ruiz, M. Biener, V. Zielasek, D. Kramer, R. Viswanath, J. Weissmüller, M. Bäumer, A. Hamza, Surface-chemistry-driven actuation in nanoporous gold, Nature Mater. 8 (1) (2009) 47–51.
[9] H.-J. Jin, X.-L. Wang, S. Parida, K. Wang, M. Seo, J. Weissmuller, Nanoporous au-pt alloys as large strain electrochemical actuators, Nano Lett. 10 (1) (2009) 187–194.
[10] X. Lang, L. Chen, P. Guan, T. Fujita, M. Chen, Geometric effect on surface enhanced raman scattering of nanoporous gold: Improving raman scattering by tailoring ligament and nanopore ratios, Appl. Phys. Lett. 94 (21) (2009) 213109.
[11] E. Detsi, Z. Chen, W. Vellinga, P. Onck, J. De Hosson, Reversible strain by physisorption in nanoporous gold, Appl. Phys. Lett. 99 (8) (2011) 083104.

[12] L. Chen, T. Fujita, M. Chen, Biofunctionalized nanoporous gold for electrochemical biosensors, Electrochim. Acta 67 (2012) 1–5.
[13] L. Gibson, Mechanical behavior of metallic foams, Ann. Rev. Mater. Sci. 30 (1) (2000) 191–227.
[14] J. Biener, A.M. Hodge, J.R. Hayes, C.A. Volkert, L.A. Zepeda-Ruiz, A.V. Hamza, F.F. Abraham, Size effects on the mechanical behavior of nanoporous au, Nano Lett. 6 (10) (2006) 2379–2382.
[15] J. Biener, A.M. Hodge, A.V. Hamza, Microscopic failure behavior of nanoporous gold, Appl. Phys. Lett. 87 (12) (2005) 121908.
[16] J. Biener, A.M. Hodge, A.V. Hamza, L.M. Hsiung, J.H. Satcher Jr, Nanoporous au: A high yield strength material, J. Appl. Phys. 97 (2) (2005) 024301.
[17] G. Pia, F. Delogu, Coarsening of nanoporous au: Relationship between structure and mechanical properties, Acta Mater. 99 (2015) 29–38.
[18] D. Farkas, A. Caro, E. Bringa, D. Crowson, Mechanical response of nanoporous gold, Acta Mater. 61 (9) (2013) 3249–3256.
[19] X.-Y. Sun, G.-K. Xu, X. Li, X.-Q. Feng, H. Gao, Mechanical properties and scaling laws of nanoporous gold, J. Appl. Phys. 113 (2) (2013) 023505.
[20] G. Pia, F. Delogu, Nanoporous au: Statistical analysis of morphological features and evaluation of their influence on the elastic deformation behavior by phenomenological modeling, Acta Mater. 85 (2015) 250–260.
[21] C.J. Ruestes, D. Farkas, A. Caro, E.M. Bringa, Hardening under compression in au foams, Acta Mater. 108 (2016) 1–7.
[22] G. Pia, M. Brun, F. Aymerich, F. Delogu, Gyroidal structures as approximants to nanoporous metal foams: clues from mechanical properties, J. Mater. Sci. 52 (2) (2017) 1106–1122.
[23] J. Jiao, N. Huber, Deformation mechanisms in nanoporous metals: Effect of ligament shape and disorder, Comput. Mater. Sci. 127 (2017) 194–203.
[24] A. Mathur, J. Erlebacher, Size dependence of effective young's modulus of nanoporous gold, Appl. Phys. Lett. 90 (6) (2007) 1910.
[25] M. Bürckert, N.J. Briot, T.J. Balk, Uniaxial compression testing of bulk nanoporous gold, Phil. Mag. 97 (15) (2017) 1157–1178.
[26] R. Viswanath, S. Polaki, R. Rajaraman, S. Abhaya, V. Chirayath, G. Amarendra, C. Sundar, On the scaling behavior of hardness with ligament diameter of nanoporous-au: Constrained motion of dislocations along the ligaments, Appl. Phys. Lett. 104 (23) (2014) 233108.
[27] L.-Z. Liu, X.-L. Ye, H.-J. Jin, Interpreting anomalous low-strength and low-stiffness of nanoporous gold: Quantification of network connectivity, Acta Mater. 118 (2016) 77–87.
[28] L.-Z. Liu, H.-J. Jin, Scaling equation for the elastic modulus of nanoporous gold with fixed network connectivity, Appl. Phys. Lett. 110 (21) (2017) 211902.
[29] K. Mangipudi, E. Epler, C. Volkert, Topology-dependent scaling laws for the stiffness and strength of nanoporous gold, Acta Mater. 119 (2016) 115–122.
[30] L.J. Gibson, M.F. Ashby, Cellular solids: Structure and Properties, Cambridge University Press, 1997.
[31] A. Hodge, J. Biener, J. Hayes, P. Bythrow, C. Volkert, A. Hamza, Scaling equation for yield strength of nanoporous open-cell foams, Acta Mater. 55 (4) (2007) 1343–1349.
[32] N.J. Briot, T. Kennerknecht, C. Eberl, T.J. Balk, Mechanical properties of bulk single crystalline nanoporous gold investigated by millimetre-scale tension and compression testing, Phil. Mag. 94 (8) (2014) 847–866.
[33] N.J. Briot, T.J. Balk, Developing scaling relations for the yield strength of nanoporous gold, Phil. Mag. (2015) 1–19.
[34] D.A. Crowson, D. Farkas, S.G. Corcoran, Geometric relaxation of nanoporous metals: The role of surface relaxation, Scripta Mater. 56 (11) (2007) 919–922.
[35] D.A. Crowson, D. Farkas, S.G. Corcoran, Mechanical stability of nanoporous metals with small ligament sizes, Scripta Mater. 61 (5) (2009) 497–499.
[36] B.-N. Ngô, B. Roschning, K. Albe, J. Weissmüller, J. Markmann, On the origin of the anomalous compliance of dealloying-derived nanoporous gold, Scripta Mater. 130 (2017) 74–77.
[37] B.-N.D. Ngô, A. Stukowski, N. Mameka, J. Markmann, K. Albe, J. Weissmüller, Anomalous compliance and early yielding of nanoporous gold, Acta Mater. 93 (2015) 144–155.
[38] J. Rodriguez-Nieva, C. Ruestes, Y. Tang, E. Bringa, Atomistic simulation of the mechanical properties of nanoporous gold, Acta Mater. 80 (2014) 67–76.
[39] Y. Sun, K.P. Kucera, S.A. Burger, T.J. Balk, Microstructure, stability and thermomechanical behavior of crack-free thin films of nanoporous gold, Scripta Mater. 58 (11) (2008) 1018–1021.
[40] Y. Sun, S.A. Burger, T.J. Balk, Controlled ligament coarsening in nanoporous gold by annealing in vacuum versus nitrogen, Phil. Mag. 94 (10) (2014) 1001–1011.
[41] A.M. Hodge, J.R. Hayes, J.A. Caro, J. Biener, A.V. Hamza, Characterization and mechanical behavior of nanoporous gold, Adv. Eng. Mater. 8 (9) (2006) 853.
[42] I. Beyerlein, A. Caro, M. Demkowicz, N. Mara, A. Misra, B. Uberuaga, Radiation damage tolerant nanomaterials, Mater. Today 16 (11) (2013) 443–449.
[43] R. Newman, S. Corcoran, J. Erlebacher, M. Aziz, K. Sieradzki, Alloy corrosion, Mrs Bull. 24 (07) (1999) 24–28.
[44] E. Bringa, J. Monk, A. Caro, A. Misra, L. Zepeda-Ruiz, M. Duchaineau, F. Abraham, M. Nastasi, S. Picraux, Y. Wang, et al., Are nanoporous materials radiation resistant?, Nano Lett 12 (7) (2011) 3351–3355.
[45] E.M. Bringa, A. Caro, Y. Wang, M. Victoria, J.M. McNaney, B.A. Remington, R.F. Smith, B.R. Torralva, H. Van Swygenhoven, Ultrahigh strength in nanocrystalline materials under shock loading, Science 309 (5742) (2005) 1838–1841.
[46] D.R. Gaston, C.J. Permann, J.W. Peterson, A.E. Slaughter, D. Andrš, Y. Wang, M.P. Short, D.M. Perez, M.R. Tonks, J. Ortensi, et al., Physics-based multiscale coupling for full core nuclear reactor simulation, Ann. Nucl. Energy 84 (2015) 45–54.
[47] R. Dou, B. Derby, Deformation mechanisms in gold nanowires and nanoporous gold, Phil. Mag. 91 (7-9) (2011) 1070–1083.
[48] https://sites.google.com/site/simafweb/proyectos/foams/
[49] S. Plimpton, Fast parallel algorithms for short-range molecular dynamics, J. Comput. Phys. 117 (1) (1995) 1–19.
[50] R. Johnson, Phase stability of fcc alloys with the embedded-atom method, Phys. Rev. B 41 (14) (1990) 9717.
[51] C.L. Kelchner, S. Plimpton, J. Hamilton, Dislocation nucleation and defect structure during surface indentation, Phys. Rev. B 58 (17) (1998) 11085.
[52] J. Alcalá, R. Dalmau, O. Franke, M. Biener, J. Biener, A. Hodge, Planar defect nucleation and annihilation mechanisms in nanocontact plasticity of metal surfaces, Phys. Rev. Lett. 109 (7) (2012) 075502.
[53] A. Stukowski, V.V. Bulatov, A. Arsenlis, Automated identification and indexing of dislocations in crystal interfaces, Modell. Simul. Mater. Sci. Eng. 20 (8) (2012) 085007.
[54] A. Stukowski, Visualization and analysis of atomistic simulation data with ovito–the open visualization tool, Modell. Simul. Mater. Sci. Eng. 18 (1) (2010) 015012.
[55] Y. Sun, J. Ye, Z. Shan, A.M. Minor, T.J. Balk, The mechanical behavior of nanoporous gold thin films, Jom 59 (9) (2007) 54–58.
[56] Y. Sun, J. Ye, A.M. Minor, T.J. Balk, In situ indentation of nanoporous gold thin films in the transmission electron microscope, Microscopy Res. Tech. 72 (3) (2009) 232–241.
[57] A. Leitner, V. Maier-Kiener, J. Jeong, M. Abad, P. Hosemann, S. Oh, D. Kiener, Interface dominated mechanical properties of ultra-fine grained and nanoporous au at elevated temperatures, Acta Mater. 121 (2016) 104–116.
[58] M. Caro, W. Mook, E. Fu, Y. Wang, C. Sheehan, E. Martinez, J. Baldwin, A. Caro, Radiation induced effects on mechanical properties of nanoporous gold foams, Appl. Phys. Lett. 104 (23) (2014) 233109.
[59] G. Ziegenhain, H.M. Urbassek, A. Hartmaier, Influence of crystal anisotropy on elastic deformation and onset of plasticity in nanoindentation: a simulational study, J. Appl. Phys. 107 (6) (2010) 061807.
[60] B. Wu, A. Heidelberg, J.J. Boland, Mechanical properties of ultrahigh-strength gold nanowires, Nature Mater. 4 (7) (2005) 525–529.
[61] C.R. Weinberger, W. Cai, Plasticity of metal nanowires, J. Mater. Chem. 22 (8) (2012) 3277–3292.
[62] M. Shaw, T. Sata, The plastic behavior of cellular materials, Int. J. Mech. Sci. 8 (7) (1966) 469–478.
[63] K. Johnson, The correlation of indentation experiments, J. Mech. Phys. Solids 18 (2) (1970) 115–126.
[64] A. Bhattacharya, W. Nix, Finite element analysis of cone indentation, Int. J. Solids Struct. 27 (8) (1991) 1047–1058.
[65] A.C. Fischer-Cripps, Introduction to Contact Mechanics, Springer, 2000.
[66] M.C. Shaw, G.J. DeSalvo, The role of elasticity in hardness testing, Metallography Microstruct. Anal. 1 (6) (2012) 310–317.
[67] Y.-T. Cheng, C.-M. Cheng, Scaling approach to conical indentation in elastic-plastic solids with work hardening, J. Appl. Phys. 84 (3) (1998) 1284–1291.
[68] M.F. Ashby, T. Evans, N.A. Fleck, J. Hutchinson, H. Wadley, L. Gibson, Metal Foams: a Design Guide, Elsevier, 2000.
[69] M. Wilsea, K. Johnson, M. Ashby, Indentation of foamed plastics, Int. J. Mech. Sci. 17 (7) (1975) 457IN5–460IN6.
[70] C. Volkert, E. Lilleodden, D. Kramer, J. Weissmüller, Approaching the theoretical strength in nanoporous au, Appl. Phys. Lett. 89 (6) (2006) 1920.
[71] L. Lührs, C. Soyarslan, J. Markmann, S. Bargmann, J. Weissmüller, Elastic and plastic poissons ratios of nanoporous gold, Scripta Mater. 110 (2016) 65–69.
[72] Y.-C. Kim, E.-J. Gwak, S.-m. Ahn, J.-i. Jang, H.N. Han, J.-Y. Kim, Indentation size effect in nanoporous gold, Acta Mater. 138 (2017) 52–60.
[73] D. Hull, D.J. Bacon, Introduction to Dislocations, vol. 257, Pergamon Press Oxford, 1984.
[74] L. Zepeda-Ruiz, E. Martinez, M. Caro, E. Fu, A. Caro, Deformation mechanisms of irradiated metallic nanofoams, Appl. Phys. Lett. 103 (3) (2013) 031909.
[75] T. Fujita, P. Guan, K. McKenna, X. Lang, A. Hirata, L. Zhang, T. Tokunaga, S. Arai, Y. Yamamoto, N. Tanaka, et al., Atomic origins of the high catalytic activity of nanoporous gold, Nature Mater. 11 (9) (2012) 775–780.
[76] J.R. Greer, W.D. Nix, Nanoscale gold pillars strengthened through dislocation starvation, Phys. Rev. B 73 (24) (2006) 245410.
[77] R. Dou, B. Derby, Strain gradients and the strength of nanoporous gold, J. Mater. Res. 25 (04) (2010) 746–753.
[78] H. Tsuzuki, P.S. Branicio, J.P. Rino, Structural characterization of deformed crystals by analysis of common atomic neighborhood, Comput. Phys. Commun. 177 (6) (2007) 518–523.
[79] A. Stukowski, K. Albe, Extracting dislocations and non-dislocation crystal defects from atomistic simulation data, Modell. Simul. Mater. Sci. Eng. 18 (8) (2010) 085001.
[80] J. Hua, A. Hartmaier, Determining burgers vectors and geometrically necessary dislocation densities from atomistic data, Modell. Simul. Mater. Sci. Eng. 18 (4) (2010) 045007.
[81] Y. Gao, C.J. Ruestes, D.R. Tramontina, H.M. Urbassek, Comparative simulation study of the structure of the plastic zone produced by nanoindentation, J. Mech. Phys. Solids 75 (2015) 58–75.
[82] C. Anders, E.M. Bringa, H.M. Urbassek, Crater production by energetic nanoparticle impact on au nanofoams, Appl. Phys. Lett. 108 (11) (2016) 113108.

[83] X.-Q. Feng, R. Xia, X. Li, B. Li, Surface effects on the elastic modulus of nanoporous materials, Appl. Phys. Lett. 94 (1) (2009) 011916.
[84] R. Xia, X. Li, Q. Qin, J. Liu, X.-Q. Feng, Surface effects on the mechanical properties of nanoporous materials, Nanotechnology 22 (26) (2011) 265714.
[85] S. Sakai, H. Tanimoto, H. Mizubayashi, Mechanical behavior of high-density nanocrystalline gold prepared by gas deposition method, Acta Mater. 47 (1) (1998) 211–217.
[86] T.J. Balk, C. Eberl, Y. Sun, K.J. Hemker, D.S. Gianola, Tensile and compressive microspecimen testing of bulk nanoporous gold, Metals Mater. Soc. 61 (12) (2009) 26–31.
[87] I.-C. Cheng, A.M. Hodge, Strength scale behavior of nanoporous ag, pd and cu foams, Scripta Mater. 69 (4) (2013) 295–298.
[88] N. Huber, R. Viswanath, N. Mameka, J. Markmann, J. Weißmüller, Scaling laws of nanoporous metals under uniaxial compression, Acta Mater. 67 (2014) 252–265.
[89] Y. Lu, J. Song, J.Y. Huang, J. Lou, Surface dislocation nucleation mediated deformation and ultrahigh strength in sub-10-nm gold nanowires, Nano Res. 4 (12) (2011) 1261–1267.
[90] K. Hu, M. Ziehmer, K. Wang, E.T. Lilleodden, Nanoporous gold: 3d structural analyses of representative volumes and their implications on scaling relations of mechanical behaviour, Phil. Mag. 96 (32-34) (2016) 3322–3335.
[91] M. Ziehmer, K. Hu, K. Wang, E.T. Lilleodden, A principle curvatures analysis of the isothermal evolution of nanoporous gold: Quantifying the characteristic length-scales, Acta Mater. 120 (2016) 24–31.
[92] E.T. Lilleodden, P.W. Voorhees, On the topological, morphological, and microstructural characterization of nanoporous metals, MRS Bull. 43 (1) (2018) 20–26.
[93] N.J. Briot, T.J. Balk, Focused ion beam characterization of deformation resulting from nanoindentation of nanoporous gold, MRS Commun. (2018) 1–5.